Ionospheric Plasma Irregularities Characterized by the Swarm Satellites: Statistics at High Latitudes

Yaqi Jin[1] , Andres Spicher[1] , Chao Xiong[2] , Lasse B. N. Clausen[1] , Guram Kervalishvili[2] , Claudia Stolle[2] , and Wojciech J. Miloch[1]

[1]Department of Physics, University of Oslo, Oslo, Norway, [2]Helmholtz Centre Potsdam, GFZ German Research Centre for Geosciences, Potsdam, Germany

Abstract The polar ionosphere is often characterized by irregularities and fluctuations in the plasma density. We present a statistical study of ionospheric plasma irregularities based on the observations from the European Space Agency's Swarm mission. The in situ electron density obtained with the Langmuir probe and the total electron content from the onboard global positioning system receiver are used to detect ionospheric plasma irregularities. We derive the irregularity parameters from the electron density in terms of the rate of change of density index and electron density gradients. We also use the rate of change of total electron content index as the irregularity parameter based on the global positioning system data. The background electron density and plasma irregularities are closely controlled by the Earth's magnetic field, with averaged enhancements close to the magnetic poles. The climatological maps in magnetic latitude/magnetic local time coordinates show predominant plasma irregularities near the dayside cusp, polar cap, and nightside auroral oval. These irregularities may be associated with large-scale plasma structures such as polar cap patches, auroral blobs, auroral particle precipitation, and the equatorward wall of the ionospheric trough. The spatial distributions of irregularities depend on the interplanetary magnetic field (IMF). By filtering the irregularity parameters according to IMF B_y, we find a clear asymmetry of the spatial distribution in the cusp and polar cap between the Northern (NH) and Southern Hemispheres (SH). For negative IMF B_y, irregularities are stronger in the dusk (dawn) sector in the NH (SH) and vice versa. This feature is in agreement with the high-latitude ionospheric convection pattern that is regulated by the IMF B_y component. The plasma irregularities are also controlled by the solar activity within the current declining solar cycle. The irregularities in the SH polar cap show a seasonal variation with higher values from September to April, while the seasonal variation in the NH is only obvious around solar maximum during 2014–2015.

1. Introduction

Ionospheric irregularities are random structures in plasma density, which give rise to inhomogeneities in the refractive index of the ionosphere. At certain spatial scales they can lead to radio wave scintillation and radar backscatter, and hence, they can impact satellite-based navigation and communication systems, which are of growing importance for our modern society (see e.g., Carlson, 2012; Kintner et al., 2007; Yeh & Liu, 1982; Tsunoda, 1988; Basu et al., 2002). Such systems depend on the quality of the received signal. The signal integrity is for example crucial for reliability and operations of global navigation satellite systems such as GPS, GLONASS, Galileo, and Beidou (Jakowski et al., 2012; Moen et al., 2013).

The global morphology of ionospheric plasma irregularities has been obtained based on ground-based observations of ionospheric scintillations (Aarons, 1982; Basu et al., 2002; Wernik et al., 2003; Yeh & Liu, 1982). Scintillations are strong at high latitudes and in the equatorial region, but usually weak at middle latitudes (Basu et al., 1988b; Basu & Groves, 2001). Compared to low and middle latitudes, studies of irregularities and resulting scintillations at high latitudes are challenging due to difficult accessibility and limited numbers of receiving stations. Recently, due to the increasing human activity in the Arctic in the last decades, the infrastructure has been improved, which resulted in new studies of space weather effects in the Arctic regions (Alfonsi et al., 2011; Clausen et al., 2016; Jin et al., 2014, 2015; Jin & Oksavik, 2018; Mitchell et al., 2005; Oksavik et al., 2015; Prikryl et al., 2010; Smith et al., 2008; Spogli et al., 2010). However, observations in the Antarctic region are still sparse and only a very few studies have been performed there (e.g., Kinrade et al., 2013; Li et al., 2010; Ngwira et al., 2010; Prikryl et al., 2011).

An important advantage of observations from polar-orbiting satellites is the data coverage over all latitudes in both hemispheres. This gives an opportunity to study plasma irregularities in a global perspective. Early satellite-based studies of plasma irregularities were mostly case studies (e.g., Basu et al., 1988a; Basu et al., 1990; Cerisier et al., 1985; Dyson et al., 1974). For example, by using power spectral analysis of in situ ion density and electric field data from the Dynamics Explorer (DE) 2 satellite, Basu et al. (1990) concluded that at least two generic classes of instabilities exist in the high-latitude ionosphere, that is, the gradient drift instability and the velocity shear-driven instability. Other studies focused on large-scale structures, that is, polar cap patches, and the associated smaller scale irregularities (Coley & Heelis, 1995, 1998b; Coley & Heelis, 1998a; Kivanc & Heelis, 1997). A few other satellite and rocket campaigns have also provided valuable information about in situ plasma structuring (Cerisier et al., 1985; Kelley et al., 1980; Kelley et al., 1982; Labelle et al., 1989; Moen et al., 2012b; Spicher et al., 2014). However, statistical studies providing global maps of ionospheric plasma irregularities using in situ techniques with the focus on high latitudes are rare. The first statistical spatial distribution of high-latitude ionospheric plasma irregularities using a polar orbiting satellite was presented by Kivanc and Heelis (1998), who showed the statistical properties of ion density and velocity structures using eight months of observations from the DE-2 satellite. The statistics were based on a power spectral analysis where the power spectral density of plasma density fluctuations at ~1-km scale was found to be higher during the interplanetary magnetic field (IMF) B_z negative and local winter. However, as they combined data from both hemispheres together by local seasons, they could not study interhemispheric asymmetries of ionospheric irregularities. Furthermore, they did not present differences in the spatial distribution with respect to the auroral oval and other related phenomena.

With the advent of the Swarm mission, several studies concerned with ionospheric structures have been conducted with the focus on high-latitude polar cap patches (Chartier et al., 2018; Goodwin et al., 2015; Spicher et al., 2015) and equatorial plasma bubbles (Rodriguez-Zuluaga et al., 2017; Wan et al., 2018; Xiong et al., 2016a; Xiong et al., 2016b), where in situ electron density measurements as well as GPS measurements were used. The GPS receiver onboard Swarm can provide the total electron content (TEC) between Swarm and GPS satellites. At low latitudes, the Swarm-based GPS TEC data have been used to characterize plasma density irregularities in the equatorial ionosphere and their influences on GPS signals (Buchert et al., 2015; Xiong et al., 2016a; Zakharenkova et al., 2016). At high latitudes, Park et al. (2017) presented the morphology of GPS TEC "perturbations" with emphasis on the orientation of plasma structures with respect to the line of sight direction. However, the statistics of the GPS TEC data and the in situ electron density data were not presented together and were not cross-compared to characterize the irregularities at high latitudes. In the present paper, we use both data sets to cross-compare the distributions of ionospheric irregularities. We define new irregularity parameters based on in situ electron density and GPS TEC data. With these parameters, we present the first comprehensive statistical results of high-latitude ionospheric plasma irregularities and their dependence on IMF configurations.

2. Data Set and Methodology

Swarm is a constellation of three identical satellites (A, B, and C) with the primary goal to study the Earth's magnetic field, upper atmosphere, and ionosphere (e.g., Friis-Christensen et al., 2006; Friis-Christensen et al., 2008; Lühr et al., 2015; Olsen et al., 2013; Stolle et al., 2013). The Swarm satellites were launched on 22 November 2013 into a polar low Earth orbit at about 500-km altitude. Between January and April 2014, Swarm B was raised to around 520-km altitude, while Swarm A and C flew side by side at an altitude of about 470 km with a difference in longitude of approximately 1.4° at the equator. Due to different precession rates, the orbital plane of Swarm B drifts gradually relative to those of Swarm A and C at a rate of approximately 1.5 hr local time per year. Each of the Swarm spacecraft carries a set of identical scientific instruments. In this study, we use data from the Electric Field Instrument and GPS receiver onboard Swarm. Furthermore, we use the magnetic field and field-aligned current (FAC) data product to derive the auroral oval boundaries, to assign our observations to given ionospheric regions (e.g., auroral oval).

The GPS receiver onboard Swarm can track up to eight GPS satellites in dual-frequency mode, and these data can be used to calculate the TEC between Swarm and the GPS satellites (e.g., van den IJssel et al., 2015). In this study, we use the Swarm Level 2 (L2) TEC data product, whose detailed description can be found at the product definition page (Swarm L2 TEC Product Description, 2017). The sampling rate of the

GPS TEC data was originally 0.1 Hz; however, the data rate was changed to 1 Hz from 16 July 2014, and thus we use only the 1-Hz GPS TEC data from that date. From the GPS TEC data, we derive parameters to characterize the fluctuations of TEC along the raypaths from Swarm to the GPS satellites. These parameters include the rate of change of TEC (ROT) and rate of change of TEC index (ROTI).

We use the vertical TEC, which we calculate from slant TEC (STEC) according to the following formula:

$$\text{TEC} = \text{STEC} \cdot \text{M}(\epsilon)$$

where M(ϵ) is a mapping function that is defined as

$$M(\in) = \frac{H}{R_{sc} + H}\left[\cos\left(\sin^{-1}(r \cdot \cos\in)\right) - r \cdot \sin\in\right]^{-1}$$

$$r = \frac{R_{sc}}{R_{sc} + H}$$

where R_{sc} is the radius of the Swarm orbit (i.e., from the Earth's center), ϵ is the elevation angle of the GPS satellite as seen from Swarm, and H is assumed to be 400 km (Foelsche & Kirchengast, 2002; Swarm L2 TEC Product Description, 2017).

ROT is the time derivative of TEC:

$$\text{ROT(t)} = \frac{\text{TEC}(t + \delta t) - \text{TEC}(t)}{\delta t}$$

where $\delta t = 1$ s, since we use the 1-Hz GPS TEC data.

ROTI is the standard deviation of ROT in a running window of 10 s:

$$\text{ROTI(t)} = \sqrt{\frac{1}{N-1}\sum_{t_i=t-\Delta t/2}^{t_i=t+\Delta t/2}\left|\text{ROT(t}_i) - \overline{\text{ROT}}\right|^2}$$

and $\overline{\text{ROT}}$ is the mean of ROT(t$_i$):

$$\overline{\text{ROT}} = \frac{1}{N}\sum_{t_i=t-\Delta t/2}^{t_i=t+\Delta t/2}\text{ROT(t}_i)$$

where $\Delta t = 10$ s, and N is the number of data points. For calculating ROT and ROTI, only the GPS satellites with elevation angles larger than 30° are used.

The Electric Field Instrument consists of two Langmuir probes (LP) from which the electron density (N_e) can be measured at a rate of 2 Hz (Knudsen et al., 2017). The in situ electron density data have been used to detect polar cap patches at high latitudes (Spicher et al., 2017). In the present study, we focus on ionospheric plasma irregularities in a general sense, without limiting ourselves to polar cap patches. We characterize ionospheric plasma irregularities with irregularity parameters derived from the electron density: the rate of change of density (ROD), rate of change of density index (RODI), and the large-scale electron density gradient (∇Ne).

ROD is defined as the time derivative of the electron density:

$$\text{ROD(t)} = \frac{Ne(t + \delta t) - Ne(t)}{\delta t}$$

Since we use the 2-Hz Swarm data for accounting for small-scale fluctuations, we use here $\delta t = 0.5$ s.

RODI is the standard deviation of ROD in a running window of 10 s:

$$\text{RODI(t)} = \sqrt{\frac{1}{N-1}\sum_{t_i=t-\Delta t/2}^{t_i=t+\Delta t/2}\left|\text{ROD(t}_i) - \overline{\text{ROD}}\right|^2}$$

where $\overline{\text{ROD}}$ is the mean of ROD(t$_i$):

$$\overline{\mathrm{ROD}} = \frac{1}{N} \sum_{t_i = t - \Delta t/2}^{t_i = t + \Delta t/2} \mathrm{ROD}(t_i)$$

where $\Delta t = 10$ s.

Besides ROD and RODI, we also calculate the large-scale density gradient (∇Ne) in a running window of 27 data points, which corresponds to a spatial scale of 100 km for Swarm. The electron density gradient is calculated using a linear regression in the running window.

These parameters form the basis of the Swarm DISC (Data, Innovation, and Science Cluster)-IPIR (Ionospheric Plasma IRregularities characterized by the Swarm satellites) product, which is a high-level global data product based on the Swarm data at all latitudes. IPIR characterizes ionospheric plasma irregularities and fluctuations in terms of their amplitudes and gradients. The data product also assigns the observations to predominant ionospheric plasma processes and regions (e.g., auroral oval, polar cap). It combines level 1B data products for Swarm: plasma density, magnetic field, L2 data products from the onboard GPS receivers, and also makes use of the L2 IBI (Ionospheric Bubble Index) product (Park et al., 2013) and the Polar Cap Products (Spicher et al., 2017). IPIR can provide comprehensive information on the morphology of plasma irregularities and fluctuations at all latitudes. This new data set makes it possible for extensive, global studies of plasma irregularities and fluctuations. In this paper, we present an example of the statistical study of high-latitude ionospheric irregularities by using the long-term Swarm IPIR data set.

3. Results

3.1. Example of High-Latitude Ionospheric Irregularities

We start with providing an example of high-latitude ionospheric irregularities based on the observations from Swarm A during 19:45–20:10 universal time (UT) on 21 December 2014, summarized in Figure 1. Figure 1a shows the ground-based GPS TEC map in magnetic latitude versus magnetic local time (MLAT-MLT) coordinates. The ground-based GPS TEC data, in bins of 1° × 1° with time resolution of 5 min, are obtained from the Madrigal database (e.g., Rideout & Coster, 2006). The Feldstein auroral oval is overlaid as solid magenta curves (Holzworth & Meng, 1975). Note that the Feldstein model only gives the statistical location of the auroral oval, while the actual auroral oval is very dynamic and its boundaries vary with respect to solar wind and geomagnetic conditions. In the example, there are several polar cap patches that can be identified in the central polar cap as regions of high TEC (~25 TECU, 1 TECU = 1×10^{16} el/m^2) in contrast to the low background TEC (~10 TECU). The high-density plasma at dayside subauroral and middle latitudes is very obvious, where the TEC values reach the maximum of the color scale (>30 TECU). The orbit of Swarm A is plotted as a black segment with timestamps annotated. As indicated by the red arrow, Swarm A is moving from the postmidnight sector through the polar cap to the afternoon sector. According to the GPS TEC map, Swarm A should encounter auroral blobs in the midnight to dawnside auroral oval near 19:50 UT, polar cap patches in the polar cap between 19:55 and 20:00 UT, low-density ionosphere in the afternoon side of the auroral oval, and high-density subauroral ionosphere slightly before 20:05 UT.

The auroral oval location is essential in characterizing plasma measurements with respect to specific phenomena and plasma processes. The aurora is associated with significant particle precipitation and FACs from the magnetosphere, which provide free energy for the development of ionospheric irregularities (Basu et al., 1990; Carlson, 2012; Clausen et al., 2016; Jin et al., 2016; Moen et al., 2012a; Tsunoda, 1988). Iijima and Potemra (1976) revealed that the FACs appear at locations closely related to the auroral oval. Therefore, by detecting FAC signatures, one can provide information about entering or exiting the auroral oval and crossing the open/closed field line boundary. The data from the vector magnetometer can be used to derive FAC, by assuming thin current sheets perpendicular to the spacecraft orbit (Lühr et al., 1996; Lühr et al., 2015; Ritter et al., 2004; Wang et al., 2005). Xiong et al. (2014) used FACs with spatial scale less than 150 km, derived from the CHAllenging Minisatellite Payload (CHAMP) spacecraft, for identifying the auroral oval boundaries and built an empirical model (Xiong & Lühr, 2014). Here we apply the same approach to the Swarm L2 FAC product to detect the auroral boundaries. Figure 1b shows the FAC data in black while the equatorward and poleward boundaries are marked with green and blue vertical lines for predawn and afternoon sectors of the auroral oval. These auroral boundaries are also included as a part of the IPIR product to assign the location of ionospheric irregularities with respect to the auroral oval. On the predawn side,
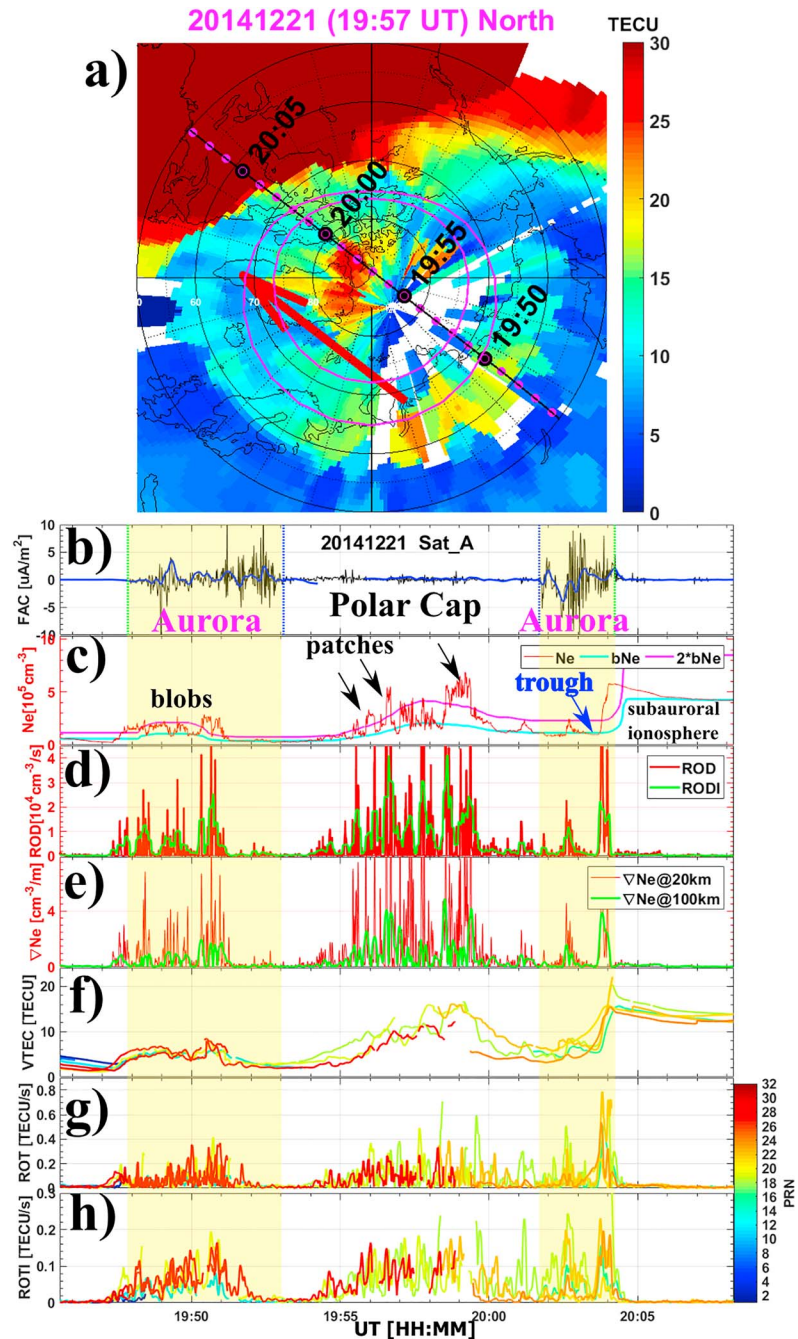
Figure 1. An example of the derived irregularity parameters from Swarm A on 21 December 2014. (a) The GPS TEC map in the northern hemisphere in a MLAT-MLT coordinate system. Noon is to the top and dawn to the right. The orbit of Swarm A is shown by a black segment and the timestamps are annotated in black dots in a cadence of 5 min. The Feldstein auroral oval is plotted in solid magenta curves. (b) The small-scale FAC derived from Swarm A (black) and the large-scale FAC derived from Swarm A and C (blue). The vertical green and blue lines show the equatorward and poleward auroral boundaries that are derived from the small-scale FAC. See text for more details. (c) The electron density (red), background electron density (bNe; cyan), and 2 times the background electron density (2* bNe; magenta). A series of polar cap patches are observed between 19:55 and 20:00 UT. (d) The rate of change of density (ROD; red) and the rate of change of density index in 10 s (RODI; black). (e) The electron density gradients (∇Ne) in a running window calculated via linear regression over 27 (5) data points for the 2-Hz electron density data, which corresponds to a spatial scale of 100 km (20 km) for Swarm. (f) GPS TEC from all available GPS satellites with the color key in the right side showing the PRN code. Only GPS satellites above the elevation angle of 30° are plotted. (g and h) Rate of change of TEC (ROT) and rate of change of TEC index in 10 s (ROTI). ROD, ROT, and ∇Ne are rectified to show their absolute values. The shaded regions present the dawnside and duskside auroral oval which are derived from the small-scale FAC data.

Swarm A passed the equatorward and poleward auroral boundaries at 19:48 UT and 19:53 UT, respectively. Swarm A crossed the duskside auroral oval during 20:02–20:04 UT. The polar cap is defined as the region between the poleward auroral boundaries, and for this case, during 19:53–20:02 UT.

The original 2-Hz electron density (N_e), the derived background density (bN_e), and twice the background density ($2*bN_e$) are presented in Figure 1c in red, cyan, and magenta, respectively. The background density is defined as the 35th percentile in a running window of about 2,000 km in length (Spicher et al., 2017). Several polar cap patches are observed inside the polar cap, where the electron density is higher than twice the background density (e.g., Crowley et al., 2000). These patches are annotated by black arrows in Figure 1c. It is clear that these high-density patches are highly structured with significantly enhanced density fluctuations. When plasma patches enter the auroral oval, they are called auroral blobs (e.g., Carlson, 1994; Carlson, 2012; Crowley et al., 2000; Jin et al., 2014). Note that auroral blobs can also be produced by soft particle precipitation which are usually associated with relatively mild density enhancements (see, e.g., Hosokawa et al., 2016; Jin et al., 2016; Carlson, 2012; Zhang et al., 2013). Several auroral blobs are observed near 19:50 UT in the postmidnight auroral oval (~3.5 MLT). By looking at the GPS TEC map from 18:30 UT to 20:00 UT (data not shown), we can confirm that these blobs are transformed from polar cap patches when they exit the nightside auroral oval. Although the density in these auroral blobs is lower than in the presented polar cap patches, their density is still above twice the background and these blobs are also highly structured. Near the afternoon side of the auroral oval, Swarm A measures a very low density plasma followed by a sharp increase in density which marks the beginning of the relatively smooth subauroral ionosphere. The low-density region is likely to be the main ionospheric trough (annotated in Figure 1c), and the sharp density increase is the equatorward wall of the trough. The equatorward wall is associated with a significant large-scale density gradient. This can be related to a study by Vo and Foster (2001), who investigated the density gradients associated with the midlatitude trough and found that the largest density gradient is often found at the equatorward wall of the trough. The ionospheric trough may be formed due to an intense sunward flow (e.g., subauroral polarization streams), which erodes the subauroral plasma due to enhanced recombination (e.g., Foster & Vo, 2002; Rodger et al., 1992; Vo & Foster, 2001). The ionospheric trough is also found to be associated with significant ionospheric irregularities and scintillations (e.g., Basu et al., 2005; Keskinen et al., 2004). In our case, the smooth subauroral ionosphere is likely structured by velocity shears and/or FAC, and small fluctuations in the density are visible. There is also one small auroral blob in the trough, where the density barely exceeds twice the background density.

Figure 1d shows ROD and RODI that were defined in section 2. Note that ROD is rectified to only show the absolute values since the magnitude of fluctuations is important for our study. Significant enhancements in both parameters are observed around auroral blobs, polar cap patches, and the equatorward wall of the ionospheric trough. This supports the use of RODI for characterizing the ionospheric plasma irregularities. At high latitudes, the large-scale (>100 km) ionospheric structures are the main sources of plasma irregularities providing density gradients, where for example, the gradient drift instability can work on to develop small-scale irregularities (e.g., Jin et al., 2014; Tsunoda, 1988). Therefore, the large-scale density gradient is also an important parameter, and we show it in Figure 1e together with the mesoscale (20 km) density gradient. The density gradient data are again rectified to show the absolute values. In the example, significant density gradients are observed during the three intervals when different large-scale plasma structures, namely, the auroral blobs, polar cap patches, and the equatorward wall of the ionospheric trough, are present.

Figure 1f shows the vertical TEC from individual GPS satellites. The advantage of the TEC data is that several (up to eight) GPS satellites can be tracked simultaneously. In Figure 1f, we only plot the TEC data with elevation angle above 30°. About four to six satellites are above 30° during the time of interest. Note that the TEC corresponds to plasma between Swarm (~470 km for Swarm A) and the GPS satellites (~20, 200 km). Therefore, the TEC from Swarm only includes the plasma density in the topside ionosphere. This is different from the usual ground-based GPS data that contains the whole profile of the ionosphere. As show in Figure 1, the TEC from the GPS receiver onboard Swarm can still reflect the variation of the ionospheric electron density. The TEC data from all GPS satellites show similar trends as the in situ electron density shown in Figure 1c, including the polar cap patches, auroral blobs, and the equatorward wall of the ionospheric trough. The three types of large-scale structures are associated with clear TEC fluctuations, which are best presented by ROT and ROTI in Figures 1g and 1h. ROT is rectified by using the absolute values.

Again, the ROT and ROTI are significantly enhanced near blobs, patches, and the equatorward wall of the trough. It should be noted that the equatorward wall of the trough is associated with very large ROT, while it is relatively lower in ROD and RODI. This indicates that the ROT is more sensitive to the density variation near the ionospheric trough.

3.2. Spatial Distribution

We first present the spatial distribution of selected irregularity parameters in geographic coordinates. The data are binned in equal-area cells in geographic latitude and geographic longitude. Each cell is approximately in size of 200 km × 400 km (about 2° in latitude × 4° in longitude at the equator). Figures 2A and 2B show the results from the LP and GPS data, respectively. The lines corresponding to MLAT (magnetic latitude) of ±60°, ±70°, and ±80° are also overlaid to indicate the geometry of the Earth's magnetic field. Due to the asymmetry of the Earth's magnetic field, the magnetic pole in the Northern Hemisphere (NH) is inclined by 7°, while the magnetic pole in the Southern Hemisphere (SH) is inclined by 16°. Note that the GPS and LP data are both from July 2014 to July 2018 to keep consistency of observations. The average electron density at high latitudes is more homogeneous in the NH than in the SH. The electron density is generally low at high latitudes except for the enhancements near the magnetic poles in both hemispheres, where the density enhancement in the SH is stronger than in the NH. Although the offsets from the magnetic poles to the geographic poles are different for both hemispheres, it is clear that the Earth's magnetic field controls the distribution of the electron density; that is, on average, the electron density is higher near the magnetic poles.

Figure 2A (c and d) shows the geographic distribution of RODI in the NH and the SH, respectively. RODI is generally low below 60° MLAT. In the NH, RODI is clearly enhanced above ~78° MLAT, while in the SH the distribution of enhanced RODI extends over a larger area and RODI is in general stronger. The distribution of the density gradient at 100-km scale is similar to RODI; that is, the area of high RODI in the NH is located above 78° MLAT, while it expands to as low as 70° MLAT in the SH.

The geographic distributions of the GPS TEC, ROT, and ROTI in Figure 2B show both similarities and differences with respect to Figure 2A. The TEC distribution in the SH is similar to the electron density distribution, while in the NH, the TEC enhancements are more distributed over north Canada and away from the NH magnetic pole as compared with N_e in the NH. ROT is largest around 80° MLAT in the NH, while it is enhanced in the whole polar cap and extends to as low as 60° MLAT in the SH. The distribution of ROTI in the NH is enhanced around 80° MLAT near longitudes close to North Canada, while it is higher in strength and larger in area in the SH where it extends toward Australia. These differences may be due to a different observation geometry, where N_e is taken from the in situ measurements at ~470 km while TEC is integrated from ~470 km upward. Note that TEC also contains plasma that is not necessarily along the same magnetic flux tube. A more detailed discussion on the geometry of GPS raypaths with respect to different plasma structures can be found in Park et al. (2017).

Figure 3 shows the spatial distributions of the plasma density (N_e and TEC) as well as the irregularity parameters in the MLAT-MLT coordinate system. The data are binned in equal-area cells in MLAT and MLT where each cell is approximately 200 km × 400 km in size (2° in latitude × 4° in longitude at the equator). The Feldstein oval is plotted as magenta curves as a reference for the statistical location of the auroral oval (Holzworth & Meng, 1975). The climatology of the electron density (Figure 3A (a and b)) is consistent with the present knowledge of the high-latitude ionosphere; that is, in both hemispheres, the electron density is high in the dayside subauroral region due to solar EUV ionization (Clausen & Moen, 2015; Jin et al., 2015; Kivanc & Heelis, 1998; Lockwood & Carlson, 1992). This high-density plasma is transported into the polar cap through the cusp throat, in agreement with the classical theory of the formation of polar cap patches (e.g., Anderson et al., 1988; Lockwood & Carlson, 1992). In the polar cap, the electron density decreases toward nightside due to slow recombination as the plasma is transported antisunward in the polar cap. Note that in summer, the whole polar cap can be illuminated by sunlight. In this situation, the plasma density in the polar cap can also be locally ionized by solar EUV. However, due to different solar zenith angles, there should still be a density gradient from the dayside toward the nightside. Note that the electron density is low near and equatorward of the nightside auroral oval (18–06 MLT). This is likely associated with the ionospheric trough, which is a region of high ion flow and low plasma density (Rodger et al., 1992). Figure 3A (c and d) shows the statistics of RODI. Unlike the electron density, RODI is very weak in the
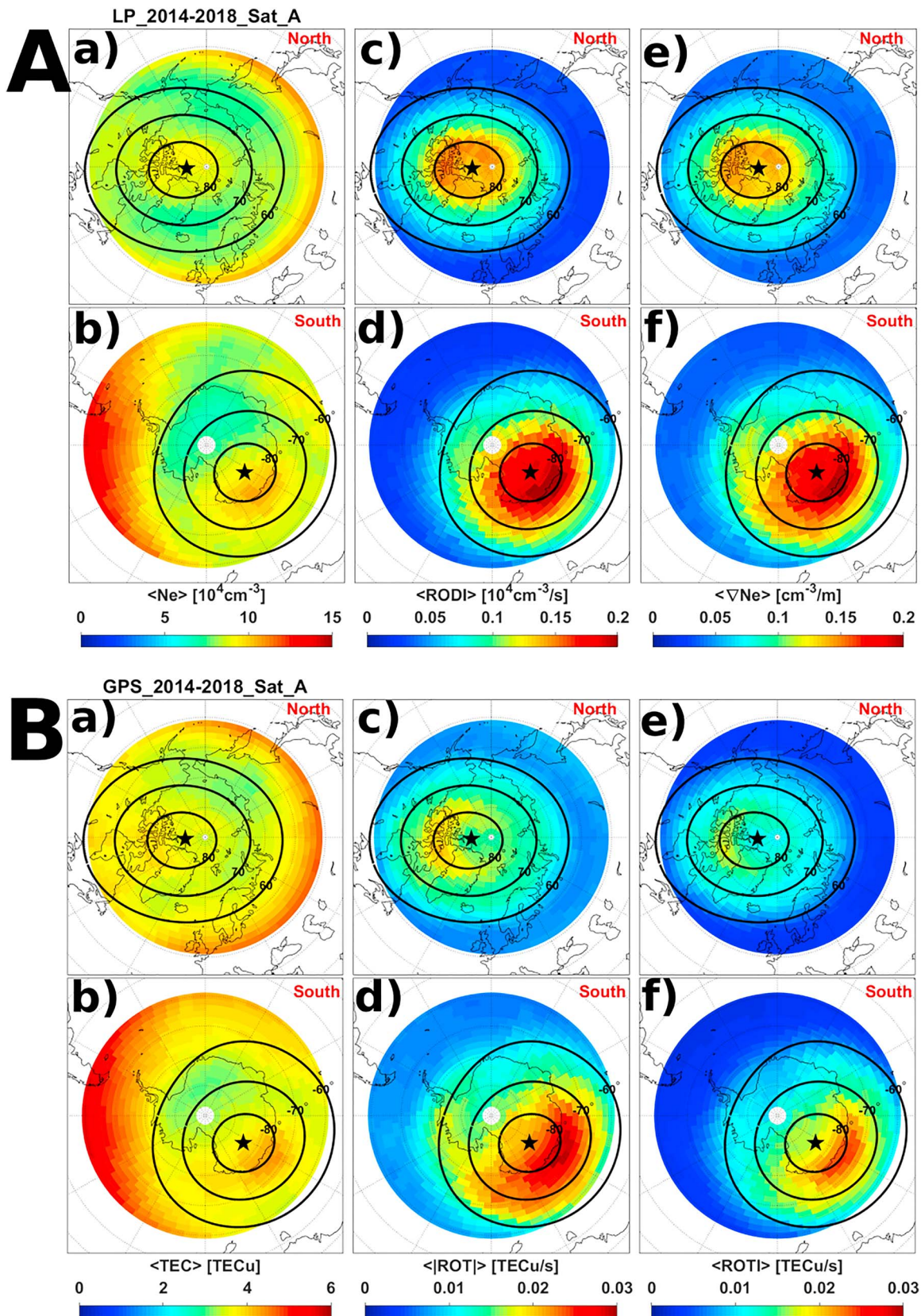
Figure 2. The geographic distribution of ionospheric irregularities using data from the (A) LP and (B) GPS. In each panel, the geomagnetic pole is shown as a black five-pointed star, and the black circles show MLAT. Only data above 50° geographic latitude are shown.
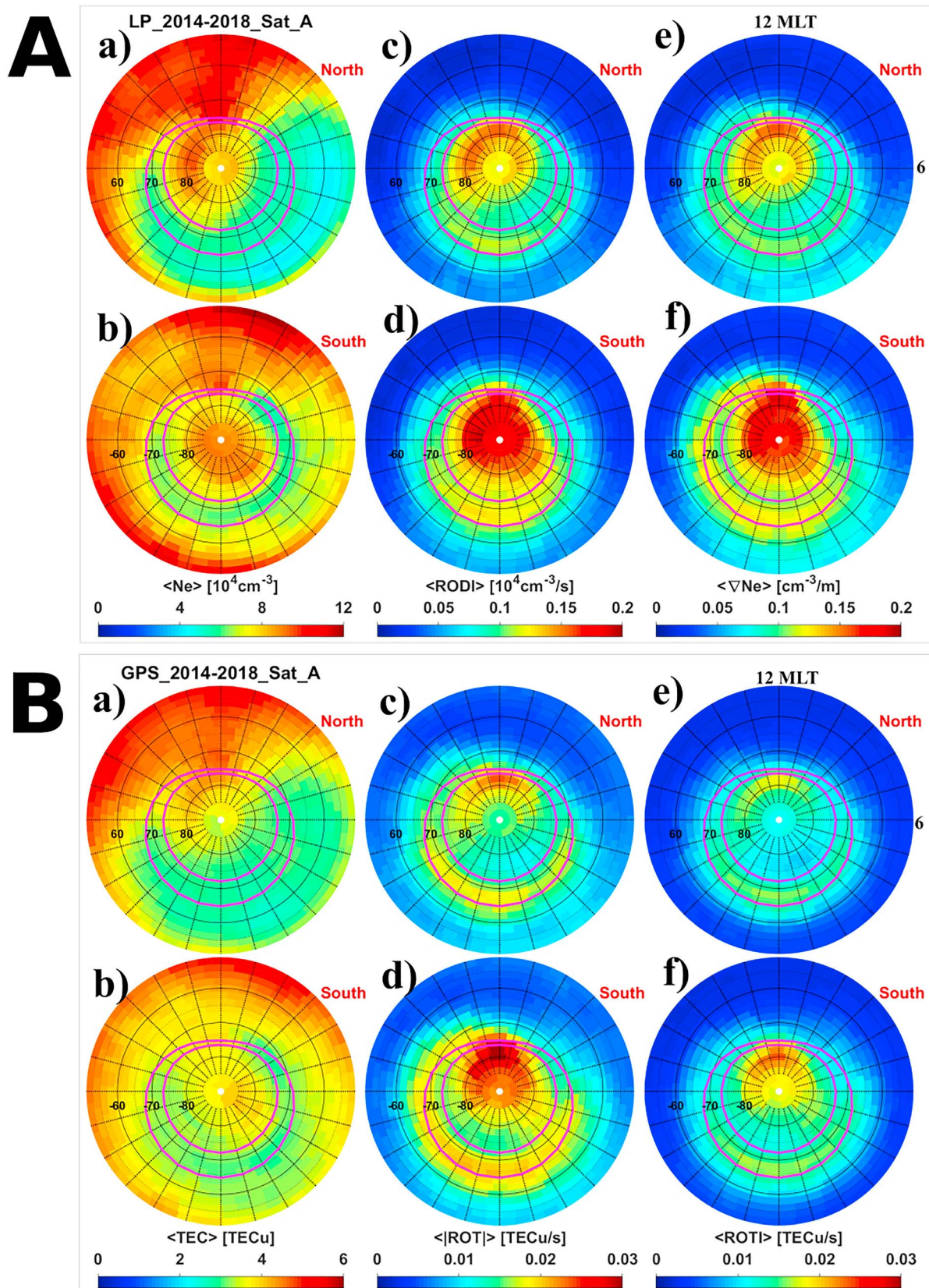
Figure 3. Climatology of plasma irregularities in MLAT-MLT coordinates using data from the (A) LP and (B) GPS. In each panel, MLT noon is to the top and dawn is to the right. The MLAT of 60°, 70°, and 80° (−60°, −70°, and − 80°) are annotated.

dayside subauroral region. It suddenly intensifies near the dayside cusp, and the area of enhanced RODI expands in local time from the cusp throat (around $\pm 75°$ MLAT) to the central polar cap. RODI decreases from the central polar cap toward the nightside auroral oval. Obvious enhancements are also visible in the nightside auroral oval (20–03 MLT). The distribution of electron density gradients at 100-km scale in Figure 3A (e and f) is similar to the one of RODI. The average density, RODI, and ∇Ne are higher in the SH when comparing to the NH. Furthermore, in the SH polar cap the distributions are much more extended from the dayside cusp toward the nightside auroral oval.

Figure 3B shows the results from the GPS measurements. The features of the TEC distribution are similar to the ones for N_e, that is, higher values in the dayside subauroral region and enhancements in the polar caps. ROT values are large between the cusp and the central polar cap and they decrease toward the nightside auroral oval. However, ROT distribution is different from RODI in the nightside auroral oval; that is, the ROT enhancements near the equatorward part of the nightside auroral oval are more significant and they are as strong as the enhancements in the polar caps. This is especially true in the SH, where ROT is enhanced from 13 MLT to 06 MLT near the equatorward boundary of the statistical auroral oval. This distribution is similar to the one of subauroral polarization streams (e.g., Foster & Vo, 2002), which can lead to fast recombination and electron density decrease. Therefore, the ROT enhancement near the equatorward part of the nightside auroral zone can be partially explained by the plasma structures near the ionospheric trough. The distributions of ROTI in Figure 3B (e and f) are similar to the distributions of RODI and the density gradients. They are also similar to the distributions of ROT except for the region near the nightside auroral oval.

3.3. IMF B_y Dependence of the Spatial Distribution

The high-latitude ionosphere is modulated by the coupling between the IMF and the Earth's magnetic field through magnetic reconnection (Cowley & Lockwood, 1992; Dungey, 1961). For example, the IMF B_y component controls the dawn-dusk asymmetry of the high-latitude convection pattern and it can influence the formation and trajectories of plasma structures (Lockwood et al., 2000; Moen et al., 2008; Zhang et al., 2011). We divide the selected parameters from Swarm according to the IMF B_y polarity, which we take from the 5-min averaged OMNI data set (King & Papitashvili, 2005). Before binning the Swarm data, the IMF data are smoothed using a moving average over 30 min. This averaging method is chosen for consistency with the previous published results (Coley & Heelis, 1998a; Moen et al., 2015; Spicher et al., 2017). The results are presented in Figures 4 and 5 for the LP and GPS data, respectively.

The subauroral plasma does not depend on the IMF B_y; that is, for each hemisphere, the distributions of N_e, RODI, and ∇Ne in the subauroral region remain the same for IMF B_y positive and negative. It is very interesting to see the asymmetry of the distribution in the cusp and polar cap in both hemispheres; that is, for IMF B_y negative, N_e, RODI, and ∇Ne are higher in the postnoon (prenoon) sector in the NH (SH), and vice versa. However, the distribution in the nightside auroral region seems to be independent of the IMF B_y polarity. We obtain similar results from the GPS data. Figure 5 shows that in the polar cap, TEC, ROT, and ROTI are higher in the postnoon (prenoon) sector in the NH (SH) for IMF B_y negative, while the distribution in the dayside subauroral region and in the nightside auroral oval are independent of the IMF B_y.

3.4. Yearly and Seasonal Variations

The yearly variations in the spatial distribution of N_e, TEC, ∇Ne, RODI, and ROTI are presented in Figures 6 and 7. Note that both LP and GPS data are from July 2014 to July 2018. The plasma density (N_e, TEC) shows similar spatial distribution as in Figure 3 during 2014–2016. Due to the declining solar cycle, the plasma density decreases dramatically from 2014 to 2018. The plasma density is very low after 2016 where only the high-density dayside ionosphere is noticeable. Changing the colorbar to a log scale does not give a significantly different result due to a significant decrease in ionospheric density from 2014 to 2018. We therefore keep the linear scale in the colorbar to be consistent with the previous figures. The electron density decreases from up to 2×10^5 cm^{-3} in 2014 to 0.5×10^5 cm^{-3} in 2018 due to very low solar activity after 2016, and TEC decreases from 10 to 4 TECU. The distributions of RODI, ∇Ne, and ROTI are similar to Figure 3, which shows enhancements around the cusp, within the polar cap and inside the nightside auroral oval. The irregularity parameters (∇Ne, RODI, and ROTI) decrease at all locations (cusp, polar cap, and nightside auroral oval) from 2014 to 2018 in a similar manner as for the background density. After 2016, irregularity parameters are still enhanced in the dayside polar cap; however, they are only perceptible around the
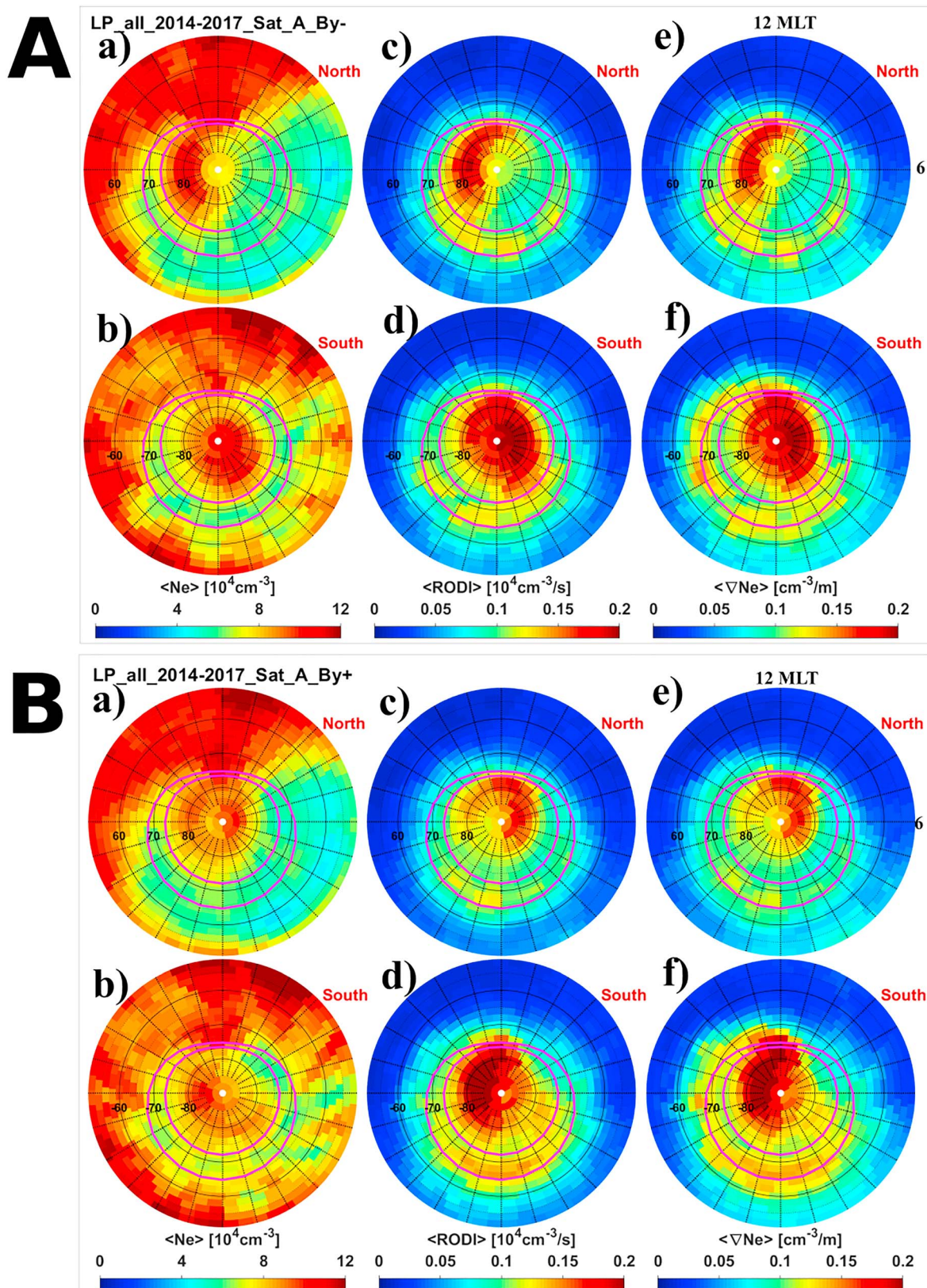
Figure 4. IMF B_y dependence of the spatial distribution for the electron density parameters. (A) IMF B_y negative and (B) IMF B_y positive. (a and b) The mean electron density, (c and d) the mean RODI in 10 s, and (e and f) the mean density gradient at 100-km scale. The first and third rows show the observation from the northern hemisphere, while the second and fourth rows are from the southern hemisphere.
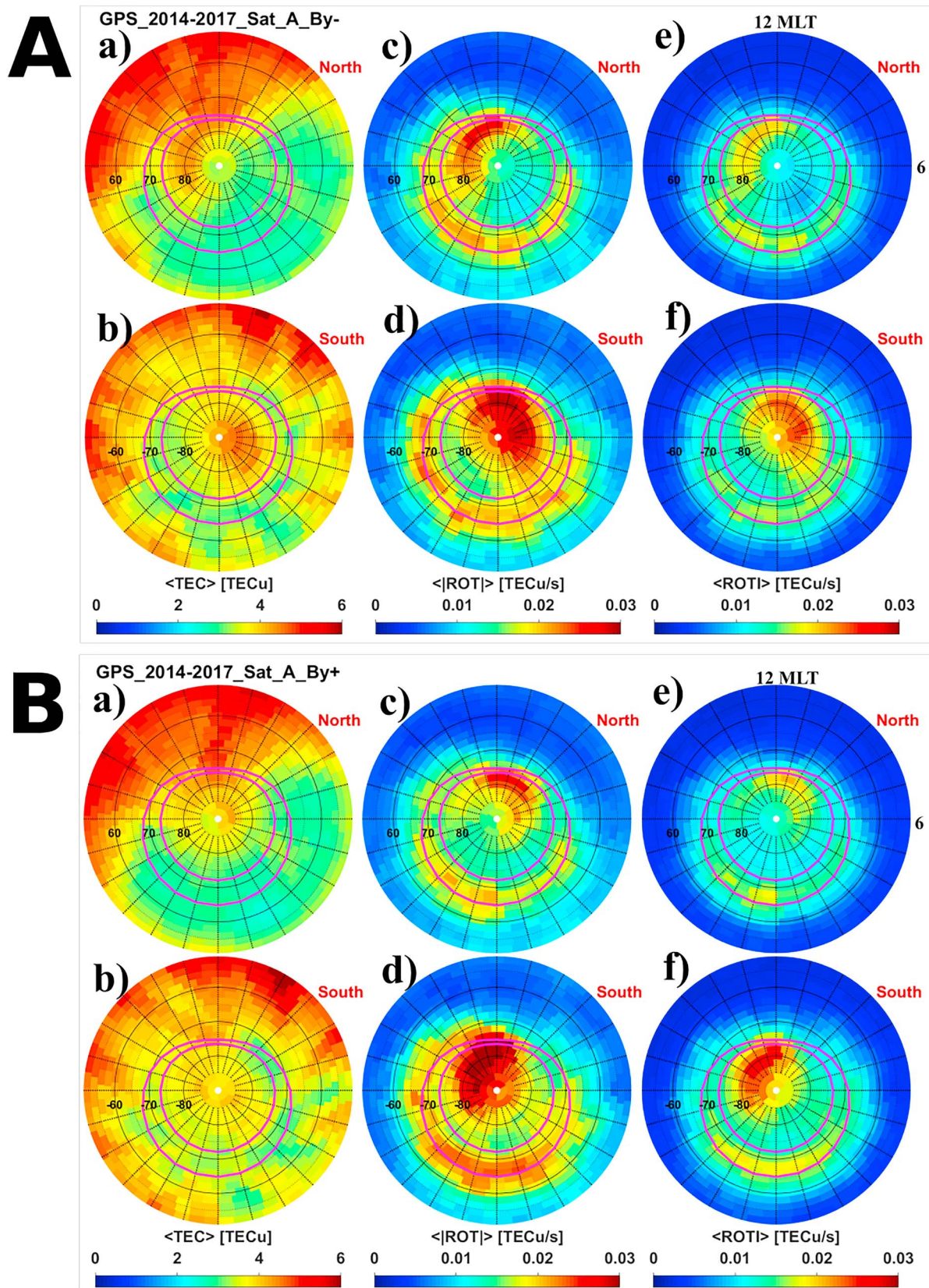
Figure 5. IMF B_y dependence of the spatial distribution for the GPS parameters. (A) IMF B_y negative and (B) IMF B_y positive. (a and b) The mean vertical TEC, (c and d) the mean ROT, and (e and f) the mean ROTI in 10 s.
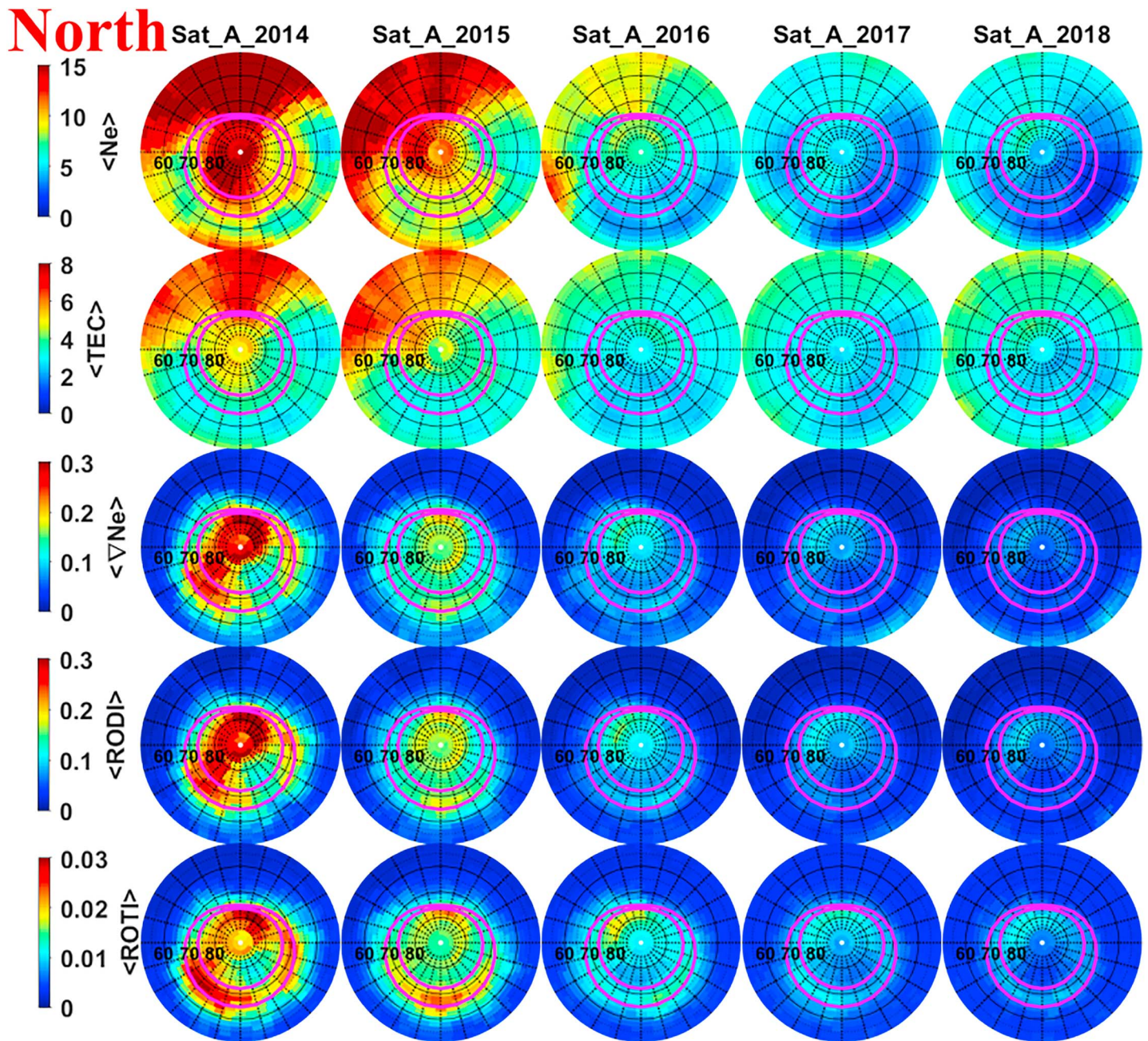
Figure 6. From top to bottom, the spatial distribution of the (first row) electron density, (second row) vertical TEC, (third row) density gradient at 100 km scale, and (fourth row) RODI and (fifth row) ROTI from 2014 to 2018 in the northern hemisphere. Each panel is presented in MLAT-MLT coordinates such that noon is to the top and dawn is to the right. The unit of each parameter is the same as the previous figures.

nightside auroral oval. The plasma density (N_e, TEC) in the SH during 2014 is more disordered, where the high-density regions can be found in the early morning and postdusk. This may be due to the fact that the data in 2014 are from July to December and Swarm uses ~131 days to complete observations for all local time sectors. See video ms01 in the supporting information for the orbital coverage of Swarm.

Swarm only covers a certain local time sector during one month, but the coverage near the central polar cap (poleward of ±81° MLAT) is very good. See videos ms01 and ms02 in the supporting information for observations and coverage of Swarm during each month. We therefore present the monthly averaged density and irregularity parameters in both polar caps in Figure 8. In the NH, the monthly averaged N_e and TEC show a well-defined semiannual variation during solar maximum in 2014–2015, that is, high ionization during
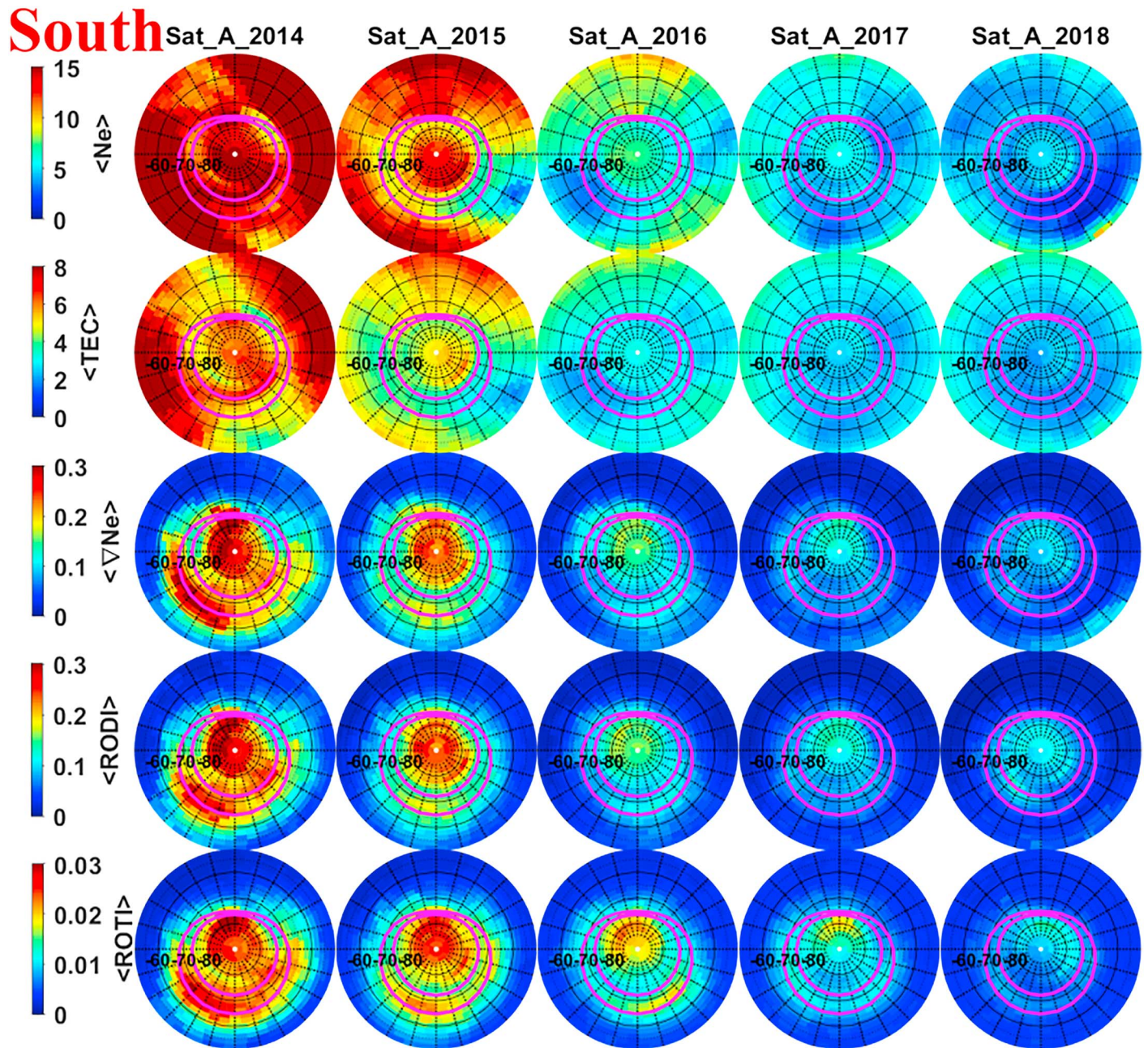
Figure 7. The spatial distribution from 2014 to 2018 for the southern hemisphere.

equinoxes and low ionization during winter and summer solstices. The seasonal variation becomes less obvious when the solar activity is becoming very low after 2016 and the plasma density behaves more like the annual variation with the high density during summer and low density during winter. The polar cap ionosphere in the SH suggests annual variation with respect to local seasons, where N_e and TEC are higher from August to April and they decrease to very low values near June solstices (local winter in the SH). It is interesting to note the intersection of the NH and the SH data near the equinoxes (March/April) when the NH and the SH have similar sunlight conditions and therefore similar ionization due to solar EUV.

Figure 8b shows the monthly averaged RODI (red) and ROTI (black). Surprisingly, RODI and ROTI in the NH and the SH show different variations with respect to local seasons. In the NH, RODI and ROTI are highest from autumn equinox (September) to spring equinox (March) with a slight decrease near the winter solstice. This variation is less pronounced when the solar activity becomes very low after 2016. The seasonal
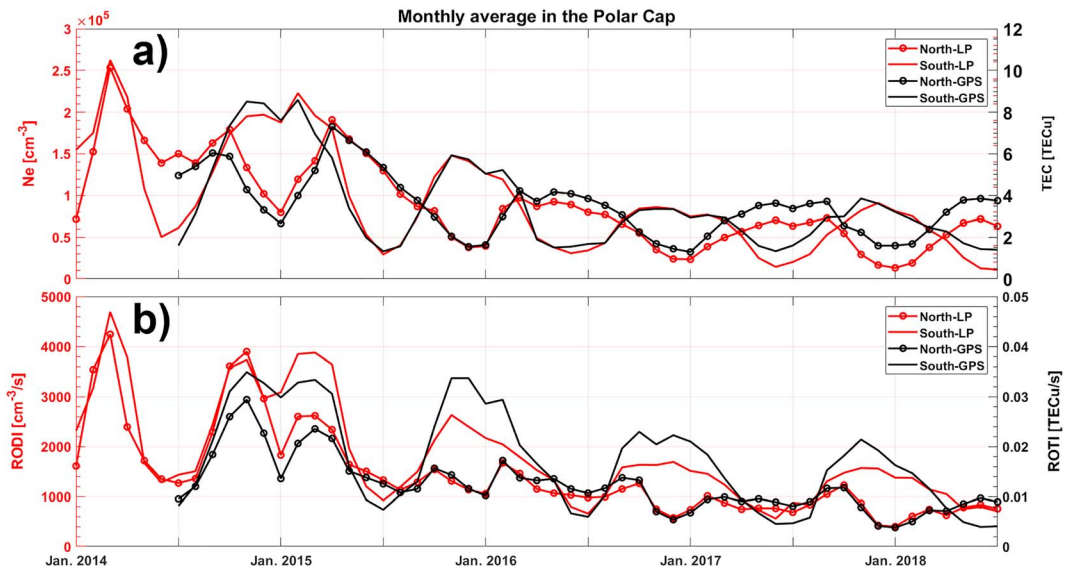
Figure 8. The seasonal variations of the ionospheric parameters from the LP (red, left axis) and GPS (black, right axis). (a) The monthly averaged electron density and vertical TEC and (b) RODI and ROTI in the central polar cap (poleward of ±81° MLAT).

variation in the SH is clear during all solar activity levels, where RODI and ROTI are highest between September and April. Note that RODI and ROTI in the SH follow the seasonal variation of the background density in Figure 8a.

4. Discussion

For the first time, we present long-term statistics of high-latitude ionospheric plasma irregularities using both in situ electron density and GPS TEC data from the Swarm mission. (A complete set of figures for the other two Swarm satellites can be found in the supporting information where the three Swarm satellites show similar spatial distributions.) The electron density and GPS TEC data give very consistent results; that is, both of them reflect the density fluctuations of large-scale structures such as polar cap patches, auroral blobs, and the ionospheric trough. The climatological maps of N_e and TEC provide an average picture of the high-latitude ionosphere showing high density in the dayside subauroral region due to the solar EUV ionization and low density in the nightside sector. Furthermore, the poleward transportation of the dayside ionosphere through the cusp throat into the polar cap is clearly captured (cf. Figure 3). This is consistent with the statistical studies based on the ground-based GPS TEC measurements in the NH (see, e.g., Yang et al., 2016; David et al., 2016; Clausen & Moen, 2015). Ground-based observations in the Antarctic are usually sparse due to a lack of ground instrumentation. However, polar orbiting satellites can observe both hemispheres with similar coverage. The climatology in the SH shows a similar spatial distribution as in the NH. However, the averaged density in the SH subauroral region is slightly disordered, where the high-density plasma spans a wider MLT range. The SH polar cap shows higher densities which extend to the nightside auroral oval. These differences could be related to the different offsets between the geographic and geomagnetic poles in the NH and the SH (e.g., Coley & Heelis, 1998a; Laundal et al., 2017; Noja et al., 2013; Rodger & Graham, 1996). We note that the altitude of Swarm A in the SH is higher by ~15 km than that in the NH. However, this small difference in the orbital altitude may not contribute too much to the interhemispheric asymmetry of the observations.

We are able to derive several irregularity parameters from the in situ electron density and GPS TEC data. The validity of these parameters is demonstrated in section 3.1. The climatological study of spatial distributions of the irregularity parameters shows enhancements around the dayside cusp, within the polar cap and in the nightside auroral oval. These results confirm previous studies of ionospheric irregularities and scintillations that were mainly based on the ground-based measurements (Basu & Groves, 2001; Basu & Valladares, 1999; Jin et al., 2014, 2015; Prikryl et al., 2015; Spogli et al., 2009). However, there are also differences between the

distribution of irregularity parameters from Swarm and the ground-based GPS scintillation measurements. The climatology of GPS scintillations highlights regions of high scintillation occurrences in the dayside cusp and the nightside auroral oval, and the scintillation occurrence is usually much lower in the polar cap (Clausen et al., 2016; Jin et al., 2015; Prikryl et al., 2015). Jin et al. (2015) reported that the dayside scintillation region is closely collocated with the cusp aurora, and the dayside polar cap immediately poleward of the cusp aurora is associated with much lower scintillation occurrences. However, the irregularity parameters from the Swarm data sets (especially RODI and ∇Ne) are also elevated in the dayside polar cap (cf. Figure 3).

The difference between the irregularity parameters derived from Swarm and ground-based GPS phase scintillation can be explained by the spatial scales of the ionospheric irregularities. As shown in section 2, RODI and ROTI are the standard deviations of ROD and ROT over 10 s, respectively. Assuming a Swarm satellite speed of 7.5 km/s, the window of 10 s corresponds to a spatial scale of 75 km. Therefore, RODI (2 Hz) characterizes spatial scales of 7.5–75 km, and ROTI (1 Hz) characterizes spatial scales of 15–75 km. Furthermore, ∇Ne corresponds to density gradients at 100 km. All these Swarm-derived irregularity parameters are sensitive to ionospheric irregularities ranging from mesoscales (10 km) to large scales (100 km), while the GPS phase scintillations from ground-based GPS receivers are sensitive to electron density irregularities of scales ranging from hundreds of meters to several kilometers (Kintner et al., 2007). In a case study, Jin et al. (2017) found that polar cap patches became less effective in producing GPS phase scintillations once they left the active cusp inflow region. However, the patches poleward of the cusp are still associated with higher levels of ROT activity (high minutely ROT values from the ground-based data). It is likely that the kilometer-scale irregularities quickly decay after they leave the cusp region, while mesoscale irregularities persist longer owing to their longer lifetime (Kelley et al., 1982; Vickrey & Kelley, 1982). These mesoscale irregularities can be transported a long way toward the nightside sector before they fade out (Kelley et al., 1982). Therefore, these mesoscale irregularities are transported by the ionospheric convection which is controlled by the IMF.

The high-latitude ionosphere is directly coupled to the solar wind and the polar ionosphere is affected by the IMF configuration. We have presented the spatial distribution of irregularity parameters under the influence of different IMF B_y configurations. The spatial distribution in the cusp and polar cap show a clear interhemispheric asymmetry; that is, for IMF B_y negative, the spatial distribution in the NH (SH) shows enhancement in the postnoon (prenoon) sectors, and vice versa. The interhemispheric asymmetry with respect to the IMF B_y is similar to the spatial distribution of the occurrences of polar cap patches (Hosokawa et al., 2006; Moen et al., 2015; Spicher et al., 2017). The asymmetry in the spatial distribution for different hemispheres with respect to the IMF B_y can be explained as follows: the high-latitude ionospheric convection pattern is controlled by the polarity of the IMF B_y (e.g., Haaland et al., 2007; Ruohoniemi & Greenwald, 2005). Under negative IMF B_y, the cusp throat is shifted toward prenoon (postnoon) in the NH (SH), and the dayside convection velocity is duskward (dawnward) in the NH (SH). The convection likely carries the large-scale plasma structures (e.g., polar cap patches) and the associated irregularities into the polar cap (see schematics in Figure 7 of Jin et al. (2015)).

Note that in the nightside auroral region, the spatial distribution is almost unchanged under different IMF B_y configurations. This is probably related to time delays of the IMF data. In this study, the IMF is averaged over 30 min, as in several previous studies (Coley & Heelis, 1998b; Moen et al., 2015; Spicher et al., 2017). The time delay from the upstream IMF to the dayside cusp is straightforward to estimate (Jin et al., 2015; Khan & Cowley, 1999). However, in order to account for the time delay due to the transit time of irregularities across the polar caps, detailed information about the convection velocity and the trajectory of irregularities is needed. Therefore, the spatial distribution in the nightside auroral zone seems to be less dependent on the IMF B_y in a statistical sense.

It is well known that ionospheric irregularities depend on the solar activity and season (Aarons et al., 1981; Basu et al., 1988b; Wernik et al., 2003). Previous scintillation studies also show high scintillation activity during the solar maximum and low activity during solar minimum (Aarons et al., 1981; Basu et al., 1988b; Jin et al., 2018). The current study clearly depicts the solar activity dependence of the electron density and irregularity parameters (cf. Figures 6 and 7); that is, the ionospheric plasma density and irregularity parameters decrease dramatically from 2014 to 2018 in response to the declining phase of the current solar cycle.

We also present the seasonal variation of irregularities in the NH and SH polar caps as monthly averaged values since the data coverage of Swarm is good in the central polar caps (above $\pm 81°$ MLAT) as compared to other regions. The averaged electron density shows clear seasonal variation in the NH near the solar maximum during 2014–2015, being lowest near winter solstices and high during summer and equinoxes. Different from the ionospheric density, RODI and ROTI in the NH are high from September to April with an obvious decrease between December and February. The general trend is similar to the seasonal distribution of polar cap patches in the NH (Coley & Heelis, 1998a; Noja et al., 2013; Spicher et al., 2017), ground-based ionospheric scintillation studies (Basu et al., 1988b; Jin et al., 2018; Li et al., 2010; Prikryl et al., 2015), and in situ irregularity power measurements by the DE-2 satellite (Kivanc & Heelis, 1998). These distributions have been explained by the effect of the sunlight. In summer, the solar EUV ionizes the ionospheric E region, which can short-circuit the F region irregularities very effectively. As a result, the F region irregularities decay quickly in the presence of a conducting E region and the irregularity amplitude is lower in the sunlit ionosphere.

In the SH, the results of ionospheric electron density and irregularity amplitude are different from the occurrences of polar cap patches in the SH (Spicher et al., 2017) and ground-based GPS scintillation by Li et al. (2010). Since the ground-based instruments are very sparse in the Antarctic regions, very few studies on ionospheric irregularities and scintillations have been conducted at high latitudes in the SH. However, from our results, the results for the SH polar cap show the same trend with respect to the calendar year as for the NH; that is, RODI and ROTI are highest from September to April and they are lowest near June solstices. This means that the NH and SH show different behaviors with respect to local seasons. The SH has stronger irregularities near a local summer (December) when the SH polar cap is illuminated by sunlight. This contradicts the explanation that the solar EUV ionized E region in summer could quickly damp F region ionospheric irregularities. It should be noted that the seasonal variation of irregularity parameters is similar to the result in Rodger and Graham (1996), which showed using the Halley HF radar in Antarctica that the occurrences of polar patches in the SH maximize during equinoxes. Around equinoxes, a tongue of enhanced ionization can be transported into the polar cap which is then structured by the auroral processes (Rodger & Graham, 1996). Furthermore, the results in the SH are also similar to the studies of polar patches by Noja et al. (2013) and Chartier et al. (2018) since they used absolute variation of the GPS TEC to define a patch (e.g., ΔTEC > 4 TECU) and our irregularity parameters are also in the absolute sense instead of relative fluctuations. However, further studies are needed to complete the understanding of the seasonal variation of ionospheric irregularities and the associated scintillation effects in the Antarctic region.

5. Summary and Concluding Remarks

From the in situ electron density and GPS TEC data based on Swarm satellites, we are able to derive several irregularity parameters that characterize density fluctuations and irregularities, namely, ROD, RODI, ∇Ne, ROT, and ROTI. In this paper, we have presented long-term (four years) statistics of high-latitude ionospheric irregularities based on these irregularity parameters. The climatological maps of the irregularity parameters agree with previous studies that are mainly based on the ground-based ionospheric scintillation studies in the NH. The irregularities show higher occurrences near the dayside cusp, polar cap, and nightside auroral oval. Furthermore, we show the spatial distribution of irregularities in the SH for the first time, which is similar to the NH. However, the ionospheric irregularities in the SH are stronger and the enhancement in the polar cap extends from the dayside cusp to the nightside auroral oval. This is likely related to the large offset between the geomagnetic and geographic poles in the SH (16°), where the ionospheric convection in the polar cap can pull in more high-density plasma.

When filtering irregularity parameters according to the IMF B_y component, we observe a clear interhemispheric asymmetry in the spatial distributions. For IMF B_y negative, the ionospheric irregularities near the cusp and in the polar cap are stronger in the postnoon (prenoon) sector in the NH (SH). The interhemispheric asymmetry is consistent with the high-latitude ionospheric convection pattern. This indicates that the IMF regulated convection pattern plays an important role in the transport and the resulting spatial distribution of ionospheric irregularities in the polar cap.

The ionospheric irregularities show a clear solar activity dependence as well as seasonal variations. Within the current declining solar cycle, the strength of ionospheric irregularities decreases dramatically from 2014

to 2018. The seasonal variations of irregularities in the polar caps show opposite results with respect to the local seasons; that is, irregularities in the NH polar cap are stronger from September to April, and they are weaker during the local summer (near June solstice), while irregularities in the SH polar cap are stronger during the local summer (around December). This is in contrast with the previous ground-based studies of ionospheric scintillations (Li et al., 2010). Further studies are needed to achieve a complete understanding on the spatial distribution and temporal variations of ionospheric irregularities in both hemispheres.

In this work, we derive irregularity parameters to characterize ionospheric irregularities globally using both in situ plasma density and GPS TEC data from Swarm. These parameters form the basis for the IPIR product. The new data set is now open to the community through http://tid.uio.no/plasma/swarm/IPIR_cdf/. This new tool allows for achieving a more complete understanding of the global distribution (spatial and temporal) of ionospheric irregularities and can take us a step forward toward space weather nowcasting/forecasting using low Earth orbiting satellites.

References

Aarons, J. (1982). Global morphology of ionospheric scintillations. *Proceedings of the IEEE*, *70*(4), 360–378. https://doi.org/10.1109/PROC.1982.12314

Aarons, J., Mullen, J. P., Whitney, H. E., Johnson, A. L., & Weber, E. J. (1981). UHF scintillation activity over polar latitudes. *Geophysical Research Letters*, *8*(3), 277–280. https://doi.org/10.1029/GL008i003p00277

Alfonsi, L., Spogli, L., De Franceschi, G., Romano, V., Aquino, M., Dodson, A., & Mitchell, C. N. (2011). Bipolar climatology of GPS ionospheric scintillation at solar minimum. *Radio Science*, *46*, RS0D05. https://doi.org/10.1029/2010RS004571

Anderson, D. N., Buchau, J., & Heelis, R. A. (1988). Origin of density enhancements in the winter polar-cap ionosphere. *Radio Science*, *23*(4), 513–519. https://doi.org/10.1029/RS023i004p00513

Basu, S., Basu, S., Mackenzie, E., Coley, W. R., Sharber, J. R., & Hoegy, W. R. (1990). Plasma structuring by the gradient drift instability at high-latitudes and comparison with velocity shear driven processes. *Journal of Geophysical Research*, *95*(A6), 7799–7818. https://doi.org/10.1029/JA095iA06p07799

Basu, S., Basu, S., Mackenzie, E., Fougere, P. F., Coley, W. R., Maynard, N. C., et al. (1988b). Simultaneous density and electric-field fluctuation spectra associated with velocity shears in the auroral oval. *Journal of Geophysical Research*, *93*(A1), 115–136. https://doi.org/10.1029/JA093iA01p00115

Basu, S., Basu, S., Makela, J. J., Sheehan, R. E., MacKenzie, E., Doherty, P., et al. (2005). Two components of ionospheric plasma structuring at midlatitudes observed during the large magnetic storm of October 30, 2003. *Geophysical Research Letters*, *32*, L12S06. https://doi.org/10.1029/2004GL021669

Basu, S., & Groves, K. M. (2001). Specification and forecasting of outages on satellite communication and navigation systems. *Space Weather*, *125*, 423–430.

Basu, S., Groves, K. M., Basu, S., & Sultan, P. J. (2002). Specification and forecasting of scintillations in communication/navigation links: Current status and future plans. *Journal of Atmospheric and Solar - Terrestrial Physics*, *64*(16), 1745–1754. https://doi.org/10.1016/S1364-6826(02)00124-4

Basu, S., Mackenzie, E., & Basu, S. (1988a). Ionospheric constraints on VHF-UHF communications links during solar maximum and minimum periods. *Radio Science*, *23*(3), 363–378. https://doi.org/10.1029/RS023i003p00363

Basu, S., & Valladares, C. (1999). Global aspects of plasma structures. *Journal of Atmospheric and Solar - Terrestrial Physics*, *61*(1–2), 127–139. https://doi.org/10.1016/S1364-6826(98)00122-9

Buchert, S., Zangerl, F., Sust, M., Andre, M., Eriksson, A., Wahlund, J. E., & Opgenoorth, H. (2015). Swarm observations of equatorial electron densities and topside GPS track losses. *Geophysical Research Letters*, *42*, 2088–2092. https://doi.org/10.1002/2015GL063121

Carlson, H. C. (1994). The dark polar ionosphere: Progress and future challenges. *Radio Science*, *29*(1), 157–165. https://doi.org/10.1029/93RS02125

Carlson, H. C. (2012). Sharpening our thinking about polar cap ionospheric patch morphology, research, and mitigation techniques. *Radio Science*, *47*, RS0L21. https://doi.org/10.1029/2011RS004946

Cerisier, J. C., Berthelier, J. J., & Beghin, C. (1985). Unstable density gradients in the high-latitude ionosphere. *Radio Science*, *20*(4), 755–761. https://doi.org/10.1029/RS020i004p00755

Chartier, A. T., Mitchell, C. N., & Miller, E. S. (2018). Annual occurrence rates of ionospheric polar cap patches observed using Swarm. *Journal of Geophysical Research: Space Physics*, *123*, 2327–2335. https://doi.org/10.1002/2017JA024811

Clausen, L. B. N., & Moen, J. I. (2015). Electron density enhancements in the polar cap during periods of dayside reconnection. *Journal of Geophysical Research: Space Physics*, *120*, 4452–4464. https://doi.org/10.1002/2015JA021188

Clausen, L. B. N., Moen, J. I., Hosokawa, K., & Holmes, J. M. (2016). GPS scintillations in the high latitudes during periods of dayside and nightside reconnection. *Journal of Geophysical Research: Space Physics*, *121*, 3293–3309. https://doi.org/10.1002/2015JA022199

Coley, W. R., & Heelis, R. A. (1995). Adaptive identification and characterization of polar ionization patches. *Journal of Geophysical Research*, *100*(A12), 23,819–23,827. https://doi.org/10.1029/95JA02700

Coley, W. R., & Heelis, R. A. (1998a). Seasonal and universal time distribution of patches in the northern and southern polar caps. *Journal of Geophysical Research*, *103*(A12), 29,229–29,237. https://doi.org/10.1029/1998JA900005

Coley, W. R., & Heelis, R. A. (1998b). Structure and occurrence of polar ionization patches. *Journal of Geophysical Research*, *103*(A2), 2201–2208. https://doi.org/10.1029/97JA03345

Cowley, S. W. H., & Lockwood, M. (1992). Excitation and decay of solar wind-driven flows in the magnetosphere-ionosphere system. *Annals of Geophysics-Atm Hydr*, *10*(1–2), 103–115.

Crowley, G., Ridley, A. J., Deist, D., Wing, S., Knipp, D. J., Emery, B. A., et al. (2000). Transformation of high-latitude ionospheric *F* region patches into blobs during the March 21, 1990, storm. *Journal of Geophysical Research*, *105*(A3), 5215–5230. https://doi.org/10.1029/1999JA900357

David, M., Sojka, J. J., Schunk, R. W., & Coster, A. J. (2016). Polar cap patches and the tongue of ionization: A survey of GPS TEC maps from 2009 to 2015. *Geophysical Research Letters*, *43*, 2422–2428. https://doi.org/10.1002/2016GL068136

Dungey, J. W. (1961). Interplanetary magnetic field and auroral zones. *Physical Review Letters*, *6*(2), 47–48. https://doi.org/10.1103/PhysRevLett.6.47

Dyson, P., McClure, J., & Hanson, W. (1974). In situ measurements of the spectral characteristics of *F* region ionospheric irregularities. *Journal of Geophysical Research*, *79*(10), 1497–1502. https://doi.org/10.1029/JA079i010p01497

Foelsche, U., & Kirchengast, G. (2002). A simple "geometric" mapping function for the hydrostatic delay at radio frequencies and assessment of its performance. *Geophysical Research Letters*, *29*(10), 1473. https://doi.org/10.1029/2001GL013744

Foster, J. C., & Vo, H. B. (2002). Average characteristics and activity dependence of the subauroral polarization stream. *Journal of Geophysical Research*, *107*(A12), 1475. https://doi.org/10.1029/2002JA009409

Friis-Christensen, E., Lühr, H., & Hulot, G. (2006). Swarm: A constellation to study the Earth's magnetic field. *Earth, Planets and Space*, *58*(4), 351–358. https://doi.org/10.1186/BF03351933

Friis-Christensen, E., Lühr, H., Knudsen, D., & Haagmans, R. (2008). Swarm: An Earth observation mission investigating geospace. *Advances in Space Research*, *41*(1), 210–216. https://doi.org/10.1016/j.asr.2006.10.008

Goodwin, L. V., Iserhienrhien, B., Miles, D. M., Patra, S., van der Meeren, C., Buchert, S. C., et al. (2015). Swarm in situ observations of *F* region polar cap patches created by cusp precipitation. *Geophysical Research Letters*, *42*, 996–1003. https://doi.org/10.1002/2014GL062610

Haaland, S. E., Paschmann, G., Forster, M., Quinn, J. M., Torbert, R. B., McIlwain, C. E., et al. (2007). High-latitude plasma convection from cluster EDI measurements: Method and IMF-dependence. *Annals of Geophysics-Germany*, *25*(1), 239–253. https://doi.org/10.5194/angeo-25-239-2007

Holzworth, R. H., & Meng, C. I. (1975). Mathematical representation of auroral oval. *Geophysical Research Letters*, *2*(9), 377–380. https://doi.org/10.1029/GL002i009p00377

Hosokawa, K., Shiokawa, K., Otsuka, Y., Nakajima, A., Ogawa, T., & Kelly, J. D. (2006). Estimating drift velocity of polar cap patches with all-sky airglow imager at Resolute Bay, Canada. *Geophysical Research Letters*, *33*, L15111. https://doi.org/10.1029/2006GL026916

Hosokawa, K., Taguchi, S., & Ogawa, Y. (2016). Periodic creation of polar cap patches from auroral transients in the cusp. *Journal of Geophysical Research: Space Physics*, *121*, 5639–5652. https://doi.org/10.1002/2015JA022221

Iijima, T., & Potemra, T. A. (1976). The amplitude distribution of field-aligned currents at northern high latitudes observed by triad. *Journal of Geophysical Research*, *81*(13), 2165–2174. https://doi.org/10.1029/JA081i013p02165

Jakowski, N., Beniguel, Y., De Franceschi, G., Pajares, M. H., Jacobsen, K. S., Stanislawska, I., et al. (2012). Monitoring, tracking and forecasting ionospheric perturbations using GNSS techniques. *Journal of Space Weather and Space*, *2*, 14. https://doi.org/10.1051/swsc/2012022

Jin, Y., Moen, J. I., & Miloch, W. J. (2014). GPS scintillation effects associated with polar cap patches and substorm auroral activity: Direct comparison. *Journal of Space Weather and Space*, *4*, A23. https://doi.org/10.1051/swsc/2014019

Jin, Y., Moen, J. I., & Miloch, W. J. (2015). On the collocation of the cusp aurora and the GPS phase scintillation: A statistical study. *Journal of Geophysical Research: Space Physics*, *120*, 9176–9191. https://doi.org/10.1002/2015JA021449

Jin, Y., Moen, J. I., Miloch, W. J., Clausen, L. B. N., & Oksavik, K. (2016). Statistical study of the GNSS phase scintillation associated with two types of auroral blobs. *Journal of Geophysical Research: Space Physics*, *121*, 4679–4697. https://doi.org/10.1002/2016JA022613

Jin, Y., Moen, J. I., Oksavik, K., Spicher, A., Clausen, L. B. N., & Miloch, W. J. (2017). GPS scintillations associated with cusp dynamics and polar cap patches. *Journal of Space Weather and Space*, *7*, A23. https://doi.org/10.1051/swsc/2017022

Jin, Y., & Oksavik, K. (2018). GPS scintillations and losses of signal lock at high latitudes during the 2015 St. Patrick's Day storm. *Journal of Geophysical Research: Space Physics*, *123*(9), 7943–7957. https://doi.org/10.1002/2018JA025933

Jin, Y. Q., Miloch, W. J., Moen, J. I., & Clausen, L. B. N. (2018). Solar cycle and seasonal variations of the GPS phase scintillation at high latitudes. *Journal of Space Weather and Space*, *8*, A48. https://doi.org/10.1051/swsc/2018034

Kelley, M. C., Baker, K. D., Ulwick, J. C., Rino, C. L., & Baron, M. J. (1980). Simultaneous rocket probe, scintillation, and incoherent-scatter radar observations of irregularities in the auroral-zone ionosphere. *Radio Science*, *15*(3), 491–505. https://doi.org/10.1029/RS015i003p00491

Kelley, M. C., Vickrey, J. F., Carlson, C. W., & Torbert, R. (1982). On the origin and spatial extent of high-latitude *F*-region irregularities. *Journal of Geophysical Research*, *87*(A6), 4469–4475. https://doi.org/10.1029/JA087iA06p04469

Keskinen, M. J., Basu, S., & Basu, S. (2004). Midlatitude sub-auroral ionospheric small scale structure during a magnetic storm. *Geophysical Research Letters*, *31*, L09811. https://doi.org/10.1029/2003GL019368

Khan, H., & Cowley, S. W. H. (1999). Observations of the response time of high-latitude ionospheric convection to variations in the interplanetary magnetic field using EISCAT and IMP-8 data. *Annals of Geophysics-Atm Hydr*, *17*(10), 1306–1335. https://doi.org/10.1007/s00585-999-1306-8

King, J. H., & Papitashvili, N. E. (2005). Solar wind spatial scales in and comparisons of hourly wind and ACE plasma and magnetic field data. *Journal of Geophysical Research*, *110*, A02104. https://doi.org/10.1029/2004JA010649

Kinrade, J., Mitchell, C. N., Smith, N. D., Ebihara, Y., Weatherwax, A. T., & Bust, G. S. (2013). GPS phase scintillation associated with optical auroral emissions: First statistical results from the geographic south pole. *Journal of Geophysical Research: Space Physics*, *118*, 2490–2502. https://doi.org/10.1002/jgra.50214

Kintner, P. M., Ledvina, B. M., & De Paula, E. R. (2007). GPS and ionospheric scintillations. *Space Weather*, *5*, S09003. https://doi.org/10.1029/2006SW000260

Kivanc, O., & Heelis, R. A. (1997). Structures in ionospheric number density and velocity associated with polar cap ionization patches. *Journal of Geophysical Research*, *102*(A1), 307–318. https://doi.org/10.1029/96JA03141

Kivanc, O., & Heelis, R. A. (1998). Spatial distribution of ionospheric plasma and field structures in the high-latitude *F* region. *Journal of Geophysical Research*, *103*(A4), 6955–6968. https://doi.org/10.1029/97JA03237

Knudsen, D. J., Burchill, J. K., Buchert, S. C., Eriksson, A. I., Gill, R., Wahlund, J. E., et al. (2017). Thermal ion imagers and Langmuir probes in the Swarm electric field instruments. *Journal of Geophysical Research: Space Physics*, *122*, 2655–2673. https://doi.org/10.1002/2016JA022571

Labelle, J., Sica, R. J., Kletzing, C., Earle, G. D., Kelley, M. C., Lummerzheim, D., et al. (1989). Ionization from soft electron-precipitation in the auroral *F*-region. *Journal of Geophysical Research*, *94*(A4), 3791–3798. https://doi.org/10.1029/JA094iA04p03791

Laundal, K. M., Cnossen, I., Milan, S. E., Haaland, S. E., Coxon, J., Pedatella, N. M., et al. (2017). North-south asymmetries in Earth's magnetic field. *Space Science Reviews*, *206*(1–4), 225–257. https://doi.org/10.1007/s11214-016-0273-0

Li, G., Ning, B. Q., Ren, Z. P., & Hu, L. H. (2010). Statistics of GPS ionospheric scintillation and irregularities over polar regions at solar minimum. *GPS Solutions*, *14*(4), 331–341. https://doi.org/10.1007/s10291-009-0156-x

Lockwood, M., & Carlson, H. C. (1992). Production of polar-cap electron-density patches by transient magnetopause reconnection. *Geophysical Research Letters*, *19*(17), 1731–1734. https://doi.org/10.1029/92GL01993

Lockwood, M., McCrea, I. W., Milan, S. E., Moen, J., Cerisier, J. C., & Thorolfsson, A. (2000). Plasma structure within poleward-moving cusp/cleft auroral transients: EISCAT Svalbard radar observations and an explanation in terms of large local time extent of events. *Annals of Geophysics-Atm Hydr*, *18*(9), 1027–1042. https://doi.org/10.1007/s00585-000-1027-5

Lühr, H., Park, J., Gjerloev, J. W., Rauberg, J., Michaelis, I., Merayo, J. M. G., & Brauer, P. (2015). Field-aligned currents' scale analysis performed with the Swarm constellation. *Geophysical Research Letters*, *42*, 1–8. https://doi.org/10.1002/2014GL062453

Lühr, H., Warnecke, J. F., & Rother, M. K. (1996). An algorithm for estimating field-aligned currents from single spacecraft magnetic field measurements: A diagnostic tool applied to Freja satellite data. *IEEE Transactions on Geoscience and Remote Sensing*, *34*(6), 1369–1376. https://doi.org/10.1109/36.544560

Mitchell, C. N., Alfonsi, L., De Franceschi, G., Lester, M., Romano, V., & Wernik, A. W. (2005). GPS TEC and scintillation measurements from the polar ionosphere during the October 2003 storm. *Geophysical Research Letters*, *32*, L12S03. https://doi.org/10.1029/2004GL021644

Moen, J., Carlson, H. C., Rinne, Y., & Skjaeveland, A. (2012a). Multi-scale features of solar terrestrial coupling in the cusp ionosphere. *Journal of Atmospheric and Solar - Terrestrial Physics*, *87-88*, 11–19. https://doi.org/10.1016/j.jastp.2011.07.002

Moen, J., Hosokawa, K., Gulbrandsen, N., & Clausen, L. B. N. (2015). On the symmetry of ionospheric polar cap patch exits around magnetic midnight. *Journal of Geophysical Research: Space Physics*, *120*, 7785–7797. https://doi.org/10.1002/2014JA020914

Moen, J., Oksavik, K., Abe, T., Lester, M., Saito, Y., Bekkeng, T. A., & Jacobsen, K. S. (2012b). First in-situ measurements of HF radar echoing targets. *Geophysical Research Letters*, *39*, L07104. https://doi.org/10.1029/2012GL051407

Moen, J., Oksavik, K., Alfonsi, L., Daabakk, Y., Romano, V., & Spogli, L. (2013). Space weather challenges of the polar cap ionosphere. *Journal of Space Weather and Space*, *3*, A02.

Moen, J., Qiu, X. C., Carlson, H. C., Fujii, R., & McCrea, I. W. (2008). On the diurnal variability in F_2-region plasma density above the EISCAT Svalbard radar. *Annals of Geophysics-Germany*, *26*(8), 2427–2433. https://doi.org/10.5194/angeo-26-2427-2008

Ngwira, C. M., McKinnell, L. A., & Cilliers, P. J. (2010). GPS phase scintillation observed over a high-latitude Antarctic station during solar minimum. *Journal of Atmospheric and Solar - Terrestrial Physics*, *72*(9–10), 718–725. https://doi.org/10.1016/j.jastp.2010.03.014

Noja, M., Stolle, C., Park, J., & Luhr, H. (2013). Long-term analysis of ionospheric polar patches based on CHAMP TEC data. *Radio Science*, *48*, 289–301. https://doi.org/10.1002/rds.20033

Oksavik, K., van der Meeren, C., Lorentzen, D. A., Baddeley, L. J., & Moen, J. (2015). Scintillation and loss of signal lock from poleward moving auroral forms in the cusp ionosphere. *Journal of Geophysical Research: Space Physics*, *120*, 9161–9175. https://doi.org/10.1002/2015JA021528

Olsen, N., Friis-Christensen, E., Floberghagen, R., Alken, P., Beggan, C. D., Chulliat, A., et al. (2013). The Swarm Satellite Constellation Application and Research Facility (SCARF) and Swarm data products. *Earth, Planets and Space*, *65*(11), 1189–1200. https://doi.org/10.5047/eps.2013.07.001

Park, J., Luhr, H., Kervalishvili, G., Rauberg, J., Stolle, C., Kwak, Y. S., & Lee, W. K. (2017). Morphology of high-latitude plasma density perturbations as deduced from the total electron content measurements onboard the Swarm constellation. *Journal of Geophysical Research: Space Physics*, *122*, 1338–1359. https://doi.org/10.1002/2016JA023086

Park, J., Noja, M., Stolle, C., & Luhr, H. (2013). The ionospheric bubble index deduced from magnetic field and plasma observations onboard Swarm. *Earth, Planets and Space*, *65*(11), 1333–1344. https://doi.org/10.5047/eps.2013.08.005

Prikryl, P., Jayachandran, P. T., Chadwick, R., & Kelly, T. D. (2015). Climatology of GPS phase scintillation at northern high latitudes for the period from 2008 to 2013. *Annals of Geophysics-Germany*, *33*(5), 531–545. https://doi.org/10.5194/angeo-33-531-2015

Prikryl, P., Jayachandran, P. T., Mushini, S. C., Pokhotelov, D., MacDougall, J. W., Donovan, E., et al. (2010). GPS TEC, scintillation and cycle slips observed at high latitudes during solar minimum. *Annals of Geophysics-Germany*, *28*(6), 1307–1316. https://doi.org/10.5194/angeo-28-1307-2010

Prikryl, P., Spogli, L., Jayachandran, P. T., Kinrade, J., Mitchell, C. N., Ning, B., et al. (2011). Interhemispheric comparison of GPS phase scintillation at high latitudes during the magnetic-cloud-induced geomagnetic storm of 5–7 April 2010. *Annals of Geophysics-Germany*, *29*(12), 2287–2304. https://doi.org/10.5194/angeo-29-2287-2011

Rideout, W., & Coster, A. (2006). Automated GPS processing for global total electron content data. *GPS Solutions*, *10*(3), 219–228. https://doi.org/10.1007/s10291-006-0029-5

Ritter, P., Lühr, H., Maus, S., & Viljanen, A. (2004). High-latitude ionospheric currents during very quiet times: Their characteristics and predictability, Paper Presented at Ann Geophys-Germany.

Rodger, A., & Graham, A. (1996). Diurnal and seasonal occurrence of polar patches, Paper Presented at Ann Geophys-Germany, Springer.

Rodger, A. S., Moffett, R. J., & Quegan, S. (1992). The role of ion drift in the formation of ionization troughs in the midlatitude and high-latitude ionosphere: A review. *Journal of Atmospheric and Terrestrial Physics*, *54*(1), 1–30. https://doi.org/10.1016/0021-9169(92)90082-V

Rodriguez-Zuluaga, J., Stolle, C., & Park, J. (2017). On the direction of the Poynting flux associated with equatorial plasma depletions as derived from Swarm. *Geophysical Research Letters*, *44*, 5884–5891. https://doi.org/10.1002/2017GL073385

Ruohoniemi, J. M., & Greenwald, R. A. (2005). Dependencies of high-latitude plasma convection: Consideration of interplanetary magnetic field, seasonal, and universal time factors in statistical patterns. *Journal of Geophysical Research*, *110*, A09204. https://doi.org/10.1029/2004JA010815

Smith, A. M., Mitchell, C. N., Watson, R. J., Meggs, R. W., Kintner, P. M., Kauristie, K., & Honary, F. (2008). GPS scintillation in the high arctic associated with an auroral arc. *Space Weather*, *6*, S03D01. https://doi.org/10.1029/2007SW000349

Spicher, A., Cameron, T., Grono, E. M., Yakymenko, K. N., Buchert, S. C., Clausen, L. B. N., et al. (2015). Observation of polar cap patches and calculation of gradient drift instability growth times: A Swarm case study. *Geophysical Research Letters*, *42*, 201–206. https://doi.org/10.1002/2014GL062590

Spicher, A., Clausen, L. B. N., Miloch, W. J., Lofstad, V., Jin, Y., & Moen, J. I. (2017). Interhemispheric study of polar cap patch occurrence based on Swarm in situ data. *Journal of Geophysical Research: Space Physics*, *122*, 3837–3851. https://doi.org/10.1002/2016JA023750

Spicher, A., Miloch, W. J., & Moen, J. I. (2014). Direct evidence of double-slope power spectra in the high-latitude ionospheric plasma. *Geophysical Research Letters*, *41*, 1406–1412. https://doi.org/10.1002/2014GL059214

Spogli, L., Alfonsi, L., De Franceschi, G., Romano, V., Aquino, M. H. O., & Dodson, A. (2009). Climatology of GPS ionospheric scintillations over high and mid-latitude European regions. *Annals of Geophysics-Germany*, *27*(9), 3429–3437. https://doi.org/10.5194/angeo-27-3429-2009

Spogli, L., Alfonsi, L., De Franceschi, G., Romano, V., Aquino, M. H. O., & Dodson, A. (2010). Climatology of GNSS ionospheric scintillation at high and mid latitudes under different solar activity conditions. *Il Nuovo Cimento B*, *125*(5–6), 623–632.

Stolle, C., Floberghagen, R., Luhr, H., Maus, S., Knudsen, D. J., Alken, P., et al. (2013). Space weather opportunities from the Swarm mission including near real time applications. *Earth, Planets and Space*, *65*(11), 1375–1383. https://doi.org/10.5047/eps.2013.10.002

Swarm L2 TEC Product Description (2017). https://earth.esa.int/documents/10174/1514862/Swarm_Level-2_TEC_Product_Description.

Tsunoda, R. T. (1988). High-latitude *F*-region irregularities: A review and synthesis. *Reviews of Geophysics*, *26*(4), 719–760. https://doi.org/10.1029/RG026i004p00719

van den IJssel, J., Encarnacao, J., Doornbos, E., & Visser, P. (2015). Precise science orbits for the Swarm satellite constellation. *Advances in Space Research*, *56*(6), 1042–1055. https://doi.org/10.1016/j.asr.2015.06.002

Vickrey, J. F., & Kelley, M. C. (1982). The effects of a conducting *E*-layer on classical *F*-region cross-field plasma-diffusion. *Journal of Geophysical Research*, *87*(A6), 4461–4468. https://doi.org/10.1029/JA087iA06p04461

Vo, H. B., & Foster, J. C. (2001). A quantitative study of ionospheric density gradients at midlatitudes. *Journal of Geophysical Research*, *106*, 21,555–21,563. https://doi.org/10.1029/2000JA000397

Wan, X., Xiong, C., Rodriguez-Zuluaga, J., Kervalishvili, G. N., Stolle, C., & Wang, H. (2018). Climatology of the occurrence rate and amplitudes of local time distinguished equatorial plasma depletions observed by Swarm satellite. *Journal of Geophysical Research: Space Physics*, *123*, 3014–3026. https://doi.org/10.1002/2017JA025072

Wang, H., Lühr, H., & Ma, S. (2005). Solar zenith angle and merging electric field control of field-aligned currents: A statistical study of the southern hemisphere. *Journal of Geophysical Research*, *110*, A03306. https://doi.org/10.1029/2004JA010530

Wernik, A., Secan, J., & Fremouw, E. (2003). Ionospheric irregularities and scintillation. *Advances in Space Research*, *31*(4), 971–981. https://doi.org/10.1016/S0273-1177(02)00795-0

Xiong, C., & Lühr, H. (2014). An empirical model of the auroral oval derived from CHAMP field-aligned current signatures: Part 2. *Annals of Geophysics-Germany*, *32*(6), 623–631. https://doi.org/10.5194/angeo-32-623-2014

Xiong, C., Luhr, H., Wang, H., & Johnsen, M. G. (2014). Determining the boundaries of the auroral oval from CHAMP field-aligned current signatures: Part 1. *Annals of Geophysics-Germany*, *32*(6), 609–622. https://doi.org/10.5194/angeo-32-609-2014

Xiong, C., Stolle, C., & Lühr, H. (2016b). The Swarm satellite loss of GPS signal and its relation to ionospheric plasma irregularities. *Space Weather*, *14*, 563–577. https://doi.org/10.1002/2016SW001439

Xiong, C., Stolle, C., Luhr, H., Park, J., Fejer, B. G., & Kervalishvili, G. N. (2016a). Scale analysis of equatorial plasma irregularities derived from Swarm constellation. *Earth, Planets and Space*, *68*(1). https://doi.org/10.1186/s40623-016-0502-5

Yang, S. G., Zhang, B. C., Fang, H. X., Kamide, Y., Li, C. Y., Liu, J. M., et al. (2016). New evidence of dayside plasma transportation over the polar cap to the prevailing dawn sector in the polar upper atmosphere for solar-maximum winter. *Journal of Geophysical Research: Space Physics*, *121*, 5626–5638. https://doi.org/10.1002/2015JA022171

Yeh, K. C., & Liu, C. H. (1982). Radiowave scintillations in the ionosphere. *Proceedings of the IEEE*, *70*(4), 324–360.

Zakharenkova, I., Astafyeva, E., & Cherniak, I. (2016). GPS and in situ Swarm observations of the equatorial plasma density irregularities in the topside ionosphere. *Earth, Planets and Space*, *68*(1). https://doi.org/10.1186/s40623-016-0490-5

Zhang, Q. H., Zhang, B. C., Moen, J., Lockwood, M., McCrea, I. W., Yang, H. G., et al. (2013). Polar cap patch segmentation of the tongue of ionization in the morning convection cell. *Geophysical Research Letters*, *40*, 2918–2922. https://doi.org/10.1002/grl.50616

Zhang, Q. H., Zhang, B. C., Liu, R. Y., Dunlop, M. W., Lockwood, M., et al. (2011). On the importance of interplanetary magnetic field vertical bar *B-y* vertical bar on polar cap patch formation. *Journal of Geophysical Research*, *116*, A05308. https://doi.org/10.1029/2010JA016287

Erratum

In the originally published version of this article, the title incorrectly read "Warm Satellites" where it should read "Swarm Satellites." This error has been corrected, and this may now be considered the authoritative version of record.